



Constitutive Behavior With Microstructure and Texture Evolution During the High-Temperature Deformation of $\text{Fe}_{11.5}\text{Co}_{20.6}\text{Ni}_{40.7}\text{Cr}_{12.2}\text{Al}_{7.8}\text{Ti}_{7.2}$ High-Entropy Alloy

PIYUSH KUMAR , M.R. RAHUL, SUMANTA SAMAL , ABHIJIT GHOSH , and GANDHAM PHANIKUMAR

Microstructure and texture evolution of the $\text{Fe}_{11.5}\text{Co}_{20.6}\text{Ni}_{40.7}\text{Cr}_{12.2}\text{Al}_{7.8}\text{Ti}_{7.2}$ (at. pct) high-entropy alloy during the high-temperature deformation has been investigated in the temperature range of 1173 K to 1373 K and strain rate of 0.1 to 0.001 s^{-1} . The stress–strain curve obtained from the deformation indicates significant flow softening at low temperatures. The softening at 1173 K is due to cracking, whereas high-temperature softening is attributed to dynamic recrystallization (DRX). Arrhenius-type sine hyperbolic relationship is used to carry out the flow stress analysis, and the predicted flow stress shows good agreement with the experimental results with an accuracy of ($R^2 = 0.955$), especially when the deformation takes place at a low strain rate. The estimated strain hardening exponent, n (> 3), and activation energy, Q ($> 400 \text{ kJ/mol}$), indicated that the deformation mechanism is dislocation controlled. Detailed microstructural and textural characterization of the hot deformed sample has been carried out using EBSD analysis. Microstructural investigation confirms that dynamic recrystallization is the primary reason behind the flow softening for the samples deformed at 1273 K and above. Strain-free recrystallized grains are found to nucleate near the grain boundary region. Furthermore, the size of the recrystallized grains increases with an increase in temperature and a decrease in strain rate. The volume fraction of the recrystallized grains is found to decrease with an increase in the Zener Holloman parameter. DRX grain was found to possess a weak texture with a low texture index.

<https://doi.org/10.1007/s11661-023-07093-x>

© The Minerals, Metals & Materials Society and ASM International 2023

I. INTRODUCTION

INITIALLY, the classical way of alloy design was based on the addition of the different alloying elements to a single principal element to get the desired properties. Recently, a new class of alloy design named high-entropy alloys (HEAs)^[1] gained much attention because of its ability to expand the range of the traditional alloying system. These HEAs are being used

in various applications in the field of defense industries, aerospace industries, and shipbuilding owing to their excellent mechanical properties.^[2] HEAs are a new class of multicomponent alloy systems, which consist of five or more principal elements in nearly equiatomic proportions or between 5 and 35 at. pct. It has received significant research interest over the past decades because of its outstanding properties, such as high-temperature strength, oxidation resistance, and thermal stability over a wide range of temperatures.^[3,4] The thermal stability in the HEAs over a wide range of temperatures is because of its high configurational entropy, which leads to the reduction of the free energy of the system and sluggish diffusion that slows the process of the different distinct phase formation and the phase transformation as well.^[2,5,6] However, a study done by Otto *et al.*^[7] and further other investigations concluded that the increase in the configurational entropy effect is inadequate to restrict the formation of the secondary phase, and other parameters, such as mixing enthalpy, play an important role in the formation of solid solution in HEAs.^[8–11] On the other hand,

PIYUSH KUMAR, SUMANTA SAMAL, and ABHIJIT GHOSH are with the Department of Metallurgical Engineering and Materials Science, Indian Institute of Technology Indore, Simrol, Indore, Madhya Pradesh, 453552, India. Contact e-mail: aghosh@iiti.ac.in M. R. RAHUL is with the Department of Fuel, Minerals, and Metallurgical Engineering, IIT (ISM) Dhanbad, Dhanbad, Jharkhand, 826004, India. GANDHAM PHANIKUMAR is with the Department of Metallurgical and Materials Engineering, Indian Institute of Technology Madras, Chennai, Tamil Nadu, 600036, India.

Manuscript submitted November 8, 2022; accepted May 4, 2023.

Article published online May 31, 2023

superalloys are considered as a perfect candidate for high-temperature applications, generally above 750 °C, because of their superior high-temperature properties along with high formability, which ease the component fabrication process.^[12,13] Furthermore, different refractory materials like Ru, Re, W, and Mo were added to the Ni-base superalloy to increase the high-temperature creep resistance of the turbine blade and so to increase the efficiency of the engine. But the refractory elements have some disadvantages like high cost and high density, especially the addition of Re can be prone to low castability and casting freckle defects in the alloys.^[4,12,14–16] In 2015, Yeh *et al.*^[17] proposed FeCoNiCrAlTi-based non-equimolar high-entropy superalloy (HESA) for high-temperature applications, which consists of a similar microstructure as Ni-based superalloy (L12(γ') embedded in FCC (γ) matrix) and found to possess comprehensive mechanical properties with few or no additions of the refractory elements. The density of HESA was below 8.0 g/cm³, which is lower as compared to Ni-based superalloy, *i.e.*, 8.5–9 g/cm³. After the discovery of the HESA by Yeh *et al.*,^[17] various investigation was performed by Tsao *et al.* regarding the microstructural stability and various high-temperature properties of the HESA, which includes the high-temperature creep and tensile properties, high-temperature hardness, oxidation, and corrosion resistance.^[4,16,18–20] Furthermore, Shiyao Chen *et al.*^[14] studied the diffusion behavior in the AlCoCrFeNiTi-based superalloys and showed that many refractory elements have lower diffusivity in this HEA system compared to Ni-base superalloy. Despite all the promising properties of FeCoNiCrAlTi HEAs, the practical applicability of this alloy depends on achieving minimum ductility or, more specifically, high-temperature flow behavior.

Although this HEA has been evaluated from different perspectives in the last few years, no study has been focused on the hot deformation behavior, specifically, microstructure and texture evolution during hot deformation in detail. Therefore, the aim of the present investigation is to understand the hot deformation behavior of FeCoNiCrAlTi alloy and the resulting microstructural and textural evolution during the deformation under a wide range of processing temperatures and strain rates. Further, a predictive model based on the Arrhenius-type sine hyperbolic relationship needs to be developed from the experimentally measured flow stress behavior.

II. EXPERIMENTAL METHOD

The dual-phase high-entropy alloy (DP-HEA) is fabricated by an arc melting process using the highly pure form of Fe, Co, Ni, Cr, Al, and Ti, with a purity level ≥ 99 pct. The nominal composition of the prepared DP-HEA is Fe_{11.5}Co_{20.6}Ni_{40.7}Cr_{12.2}Al_{7.8}Ti_{7.2} (at. pct). The ingot was prepared using an arc melting route under the highly pure argon atmosphere of purity level ≥ 99.7 pct. The ingot was remelted five times to ensure the chemical homogeneity of the alloying elements during

the liquid phase. Furthermore, the button-shaped ingot, which was prepared from the arc melting route, was suction cast in a cylindrical rod of diameter 6 mm using the water-cooled Cu split mold. To understand the high-temperature deformation behavior of the prepared alloy, the cylindrical specimen of diameter $\varnothing = 6$ mm and length 9 mm was taken out from the suction-cast cylindrical rod. The isothermal compression test was performed on the specimen using Gleeble @ 3800 thermomechanical simulator within the temperature range of 900 °C to 1100 °C (1173 K to 1373 K) and strain rate varying from 0.001 s⁻¹ to 0.1 s⁻¹. The sample was heated at the rate of 5 K/s to reach the desired temperature and held for 5 min at that temperature to ensure the homogeneous distribution of temperature throughout the specimen before the initiation of compression. After the sample was compressed up to 0.6 true strain, the compressed specimen was rapidly cooled to retain its deformed microstructure. As the samples cooled down, it was cut into two parts along the compression axis, and the microstructure analysis was carried out along that (See electronic supplementary Figure S1 for a schematic illustration). Furthermore, to identify the texture of the deformed specimens, the electron backscattered diffraction (EBSD) analysis was carried out, for which the sample was polished following standard metallographic techniques, followed by 0.05 μ m-sized colloidal silica suspension. For the data Acquisition, AzTec software by oxford instrument was used, the data were exported in.ctf and.cpr format for the analysis, and HKL channel 5 system software, as well as MTEX toolbox in MATLAB software, was used for the processing of data. The separation of the recrystallized and non-recrystallized grains was done based on the grain orientation spread (GOS < 0.1).

III. RESULT AND DISCUSSION

A. Stress–Strain Curves

The engineering stress–strain curves obtained from the hot deformation at various strain rate and temperature are shown in Figure 1. Flow stress is found to decrease with an increase in temperature at a particular strain rate, whereas flow stress increases with the increase in the strain rate at a constant temperature. In all the flow curves, flow softening phenomena become dominant after an initial short hardening period. Work hardening may have contributed to the initial flow hardening. As expected, the peak stress value is found to be strongly dependent on the deformation temperature. In case of deformation at 1173 K temperature, the softening effect is severe. At 0.1 s⁻¹ strain rate, the flow curve drops down to 400 MPa stress value at 0.4 engineering strain from 900 MPa peak stress value. In order to identify this abnormal softening effect, the microstructures of the hot deformed samples after 0.6 true strain, followed by water quenching, have been studied at low magnification under SEM and are shown in Figure 2. Interestingly, major cracks, as shown by the arrow in Figure 2, are found to develop in the region

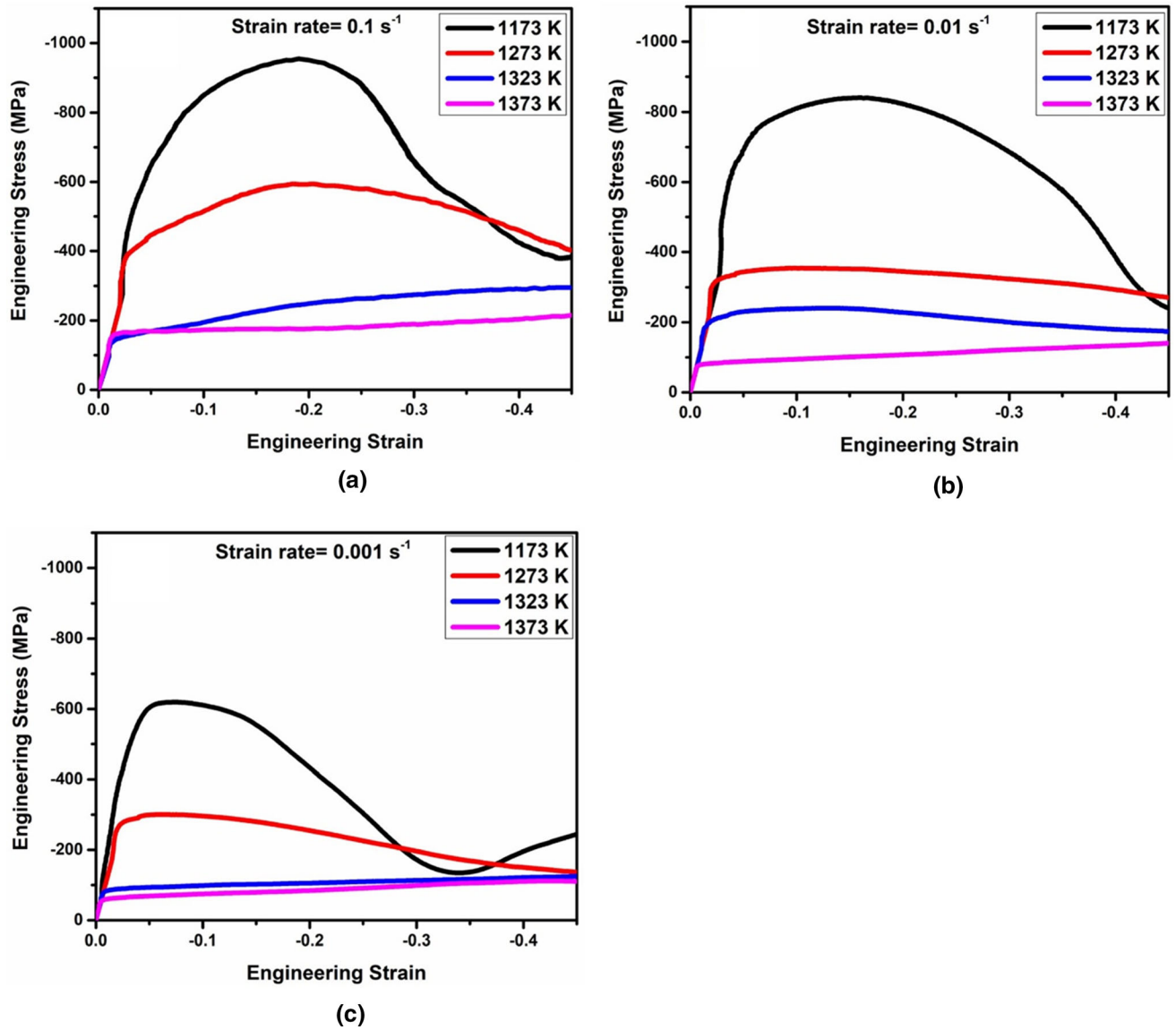


Fig. 1—Engineering stress vs Engineering strain plot of FeCoNiCrAlTi DP-HEA for different temperatures and strain rate (a) 0.1 s^{-1} (b) 0.01 s^{-1} (c) 0.001 s^{-1} .

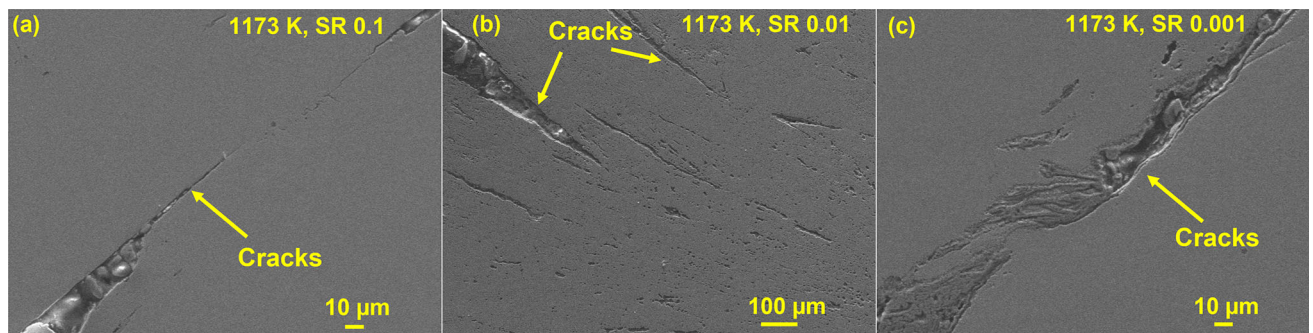


Fig. 2—Cracks developed during the deformation at the following parameters (a) 1173 K SR0.1 (b) 1173 K SR0.01 (c) 1173 K SR0.001.

close to the center of samples deformed at 1173 K. The softening behavior observed at other deformation temperature may have other reasons, which is discussed in

detail in the latter section. Recently, Reliance *et al.*^[21] depicted the deformation behavior of a single-phase FCC CoCrFeNiV high-entropy alloy in the temperature

range of 1073 K to 1373 K at a strain rate of 0.1 s^{-1} . In that study, except for the sample deformed at 1073 K, all other samples exhibit similar behavior, *i.e.*, exhibiting a peak strength followed by a steady strength value as deformation progress. In the case of low-temperature deformation (1073 K to 1173 K), deformation bands evolved, whereas the formation of annealing twins was reported in the case of high-temperature deformation (1273 K to 1373 K). At 1173 K and 1273 K, the observed peak stress is approximately twice in the present alloy as compared to the single-phase FCC CoCrFeNiV high entropy. However, at 1373 K, approximately 20 pct lower peak stress has been observed in the present investigation compared to the single-phase FCC CoCrFeNiV high-entropy alloy. For further analysis, the engineering stress–strain is converted into true stress–strain by using the following formula:

$$\sigma_{\text{True}} = \sigma_{\text{Engg}} (\epsilon_{\text{Engg}} + 1) \quad \text{[(i)]}$$

$$\epsilon_{\text{True}} = \ln(\epsilon_{\text{Engg}} + 1) \quad \text{[(ii)]}$$

where σ_{True} denotes the true stress, σ_{Engg} denotes the engineering stress, ϵ_{Engg} denotes engineering strain and ϵ_{True} denotes true strain.

B. Modeling of Flow Curves and Calculation of Hot Deformation Parameters

Flow stress of the material during high-temperature deformation is affected by the strain, strain rate, and deformation temperature, and the relationship between the parameters is expressed by using an appropriate constitutive equation. Here, the flow analysis is carried out using the Arrhenius-type hyperbolic sine relationship.

$$\dot{\epsilon} = A \times [\sinh(\alpha\sigma)]^n \times \exp\left(\frac{-Q}{RT}\right) \quad [1]$$

where A is a material constant, Q is the activation energy in J/mol, R is the universal gas constant 8.314 J/mol-K, T is the deformation temperature in K, σ is the deformation stress in MPa, $\dot{\epsilon}$ is the strain rate in s^{-1} , A , n , and α are material constants in which $\alpha = \frac{\beta}{N}$.

Furthermore, the effect of the parameters like temperature and strain rate during hot working conditions can be combined using Zener–Holloman Parameter (Z),^[22,23] and it is defined as:

$$Z = A \times [\sinh(\alpha\sigma)]^n = \dot{\epsilon} \times \exp\left(\frac{Q}{RT}\right) \quad [2]$$

Here, Q is the activation energy in J/mol, R is the universal gas constant 8.314 J/mol-K, T is the deformation temperature in K, σ is the deformation stress in MPa, $\dot{\epsilon}$ is the strain rate in s^{-1} , A , n , and α are material constants in which $\alpha = \frac{\beta}{N}$.

Now, taking the natural logarithm of Eq. [1], it can be written as:

$$\frac{1}{n} \ln(\dot{\epsilon}) + \frac{1}{n} \left(\frac{Q}{RT}\right) - \frac{1}{n} \ln A = \ln[\sinh(\alpha\sigma)]^n \quad [3]$$

Furthermore, the following equation can be derived by the partial differentiation of Eq. [3].

$$n = \frac{d(\ln(\dot{\epsilon}))}{d(\ln(\sinh(\alpha\sigma)))} \quad [4]$$

Hence from Eq. [4], the value of ‘ n ’ can be determined by taking the average of the slope of lines to form the plot of $\ln(\dot{\epsilon})$ vs $\ln(\sinh(\alpha\sigma))$ as shown in Figure 3(c).

Similarly, the activation energy Q can also be calculated by taking the partial differentiation of Eq. [3], and it is as follows:

$$Q = Rn \frac{d(\ln(\sinh(\alpha\sigma)))}{d(1/T)} \quad [5]$$

It is also be written as $Q = 10,000 \times R \times n \times s$.

Here, s is the slope of the linear fit of the plot between $10,000/T$ vs $\ln(\sinh(\alpha\sigma))$ as shown in Figure 3(d). Similarly, the different material constants can be calculated by linear fitting of different plots. The value of β can be calculated from the slope of the plot between σ vs $\ln(\dot{\epsilon})$ and the values of N can be calculated from the slope of the plot between $\ln\sigma$ vs $\ln(\dot{\epsilon})$ as shown in Figures 3(a) and (b).

The material constant A can also be calculated by taking the natural logarithm of Eq. [2], which can be expressed as

$$\ln(Z) = \ln(A) + n \times \ln(\sinh(\alpha\sigma)) \quad [6]$$

from Eq. [6], the intercept in the plot between $\ln(Z)$ vs $\ln(\sinh(\alpha\sigma))$ will give the value of ‘ A ’ as shown in Figure 3(e).

It is worth to be mentioned here that a severe through-thickness crack evolved during the deformation at 1173 K results in unusual flow behavior, and thus, the flow curves obtained at 1173 K are excluded from the model prediction.

Finally, the flow stress as a function of strain, strain rate, and temperature can be predicted using the following Arrhenius model:

$$\sigma = \frac{1}{\alpha} \ln \left(\left(\frac{Z}{A}\right)^{\frac{1}{n}} + \left(\left(\frac{Z}{A}\right)^{\frac{2}{n}} + 1\right)^{\frac{1}{2}} \right) \quad [7]$$

Various model parameters have been estimated by fitting the constitutive model at every 0.05 strain interval and are listed in Table I.

The value of different parameters Z , σ , and $\dot{\epsilon}$ calculated at strain 0.6 is expressed by the following equation:

$$Z_{0.6} = \dot{\epsilon} \exp\left(\frac{433253}{RT}\right) \quad [8]$$

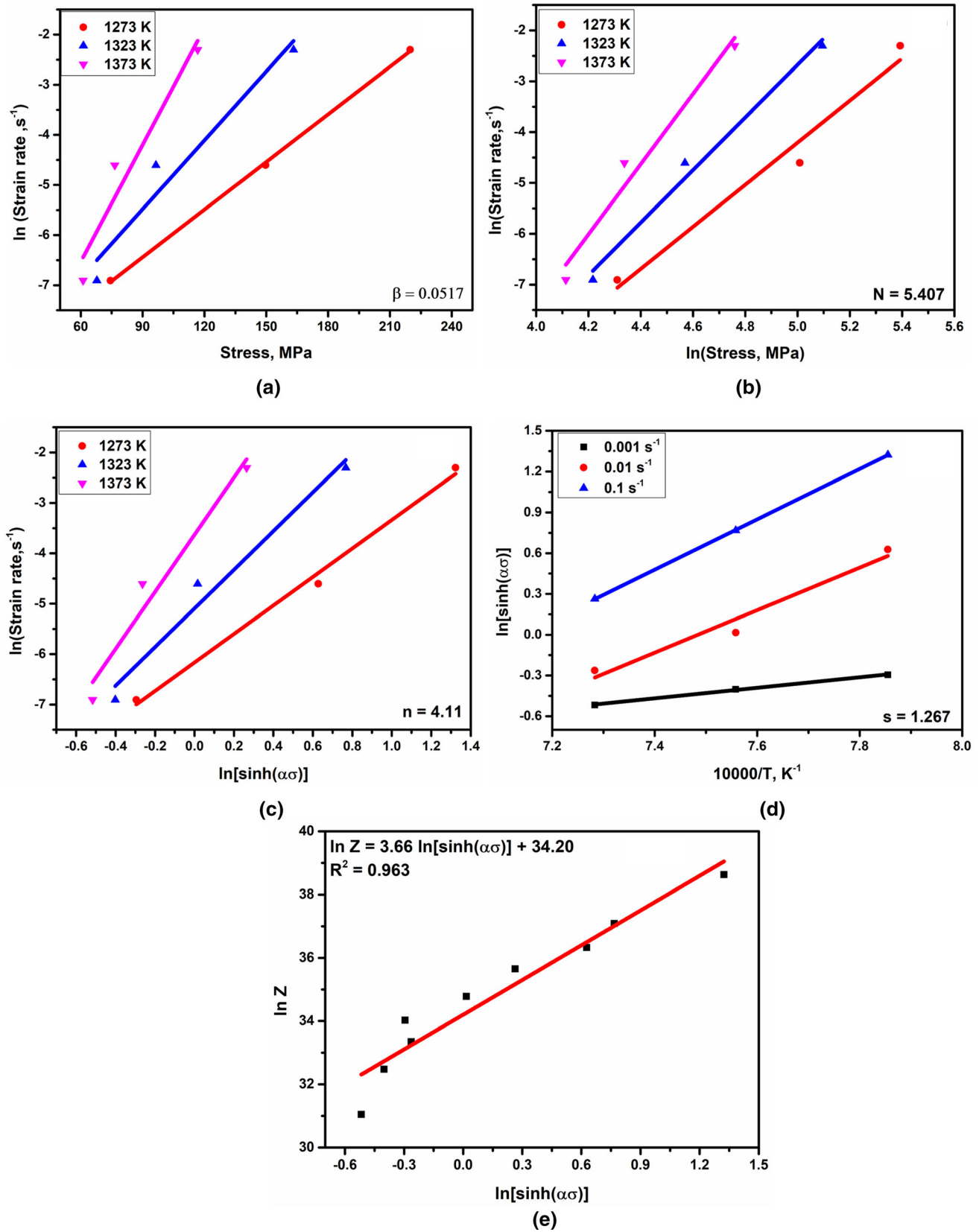


Fig. 3—Calculation of parameters at strain 0.6 (a) β (b) N (c) n (d) s (e) $\ln Z$.

Table I. Estimated Model Parameters

Strain	N	β	α	n	s	Q	$\ln A$
0.05	6.392243	0.031193	0.005939	3.916657	3.224773	1050.085	89.918
0.1	5.688553	0.030767	0.006061	3.639797	3.272127	990.1870	84.329
0.15	5.306033	0.03234	0.006365	3.542467	3.325837	979.527	83.198
0.2	5.257193	0.035017	0.006688	3.6142	3.2667	981.593	83.323
0.25	5.312077	0.03726	0.00687	3.749683	3.039387	947.524	80.29
0.3	5.332643	0.03935	0.007111	3.84669	2.765873	884.5644	74.68
0.35	5.4547	0.041773	0.007287	4.015707	2.4697	824.5484	69.376
0.4	5.376777	0.043197	0.007597	4.022067	2.211187	739.4089	61.774
0.45	5.440933	0.045417	0.007902	4.104823	1.926253	657.38212	54.405
0.5	5.509537	0.047527	0.008199	4.1845	1.669857	580.9420	47.578
0.55	5.538333	0.050123	0.00867	4.206667	1.4604	510.76360	41.21
0.6	5.407857	0.051743	0.009252	4.110397	1.267793	433.25363	34.202

$$\dot{\epsilon} = 7.14 \times 10^{14} \times [\sinh(0.009252 \times \sigma_{0.6})]^{4.11} \times \exp\left(\frac{433253}{RT}\right) \quad [9]$$

$$\sigma_{0.6} = \frac{1}{0.009252} \ln\left(\left(\frac{Z_{0.6}}{7.14 \times 10^{14}}\right)^{\frac{1}{4.11}} + \left(\left(\frac{Z_{0.6}}{7.14 \times 10^{14}}\right)^{\frac{1}{4.11}} + 1\right)^{\frac{1}{2}}\right) \quad [10]$$

Here, the relationship obtained from Eq. [10] helps in predicting the required flow stress at a given true strain (here, it is 0.6), temperature, and strain rate during the metalworking process.

Hence, the dependence of material parameters such as ‘ Q ’ and ‘ n ’ on different strains is established by using the above equations. The polynomial relationships are given below:

$$Q = 1045.67 - 97.80\epsilon + (-1591.9)\epsilon^2$$

$$n = 4.15 - 7.31\epsilon + (29.04)\epsilon^2 + (-28.4)\epsilon^3$$

Finally, the flow curve has been predicted from the material constants and the Arrhenius model estimated above over the wide range of strain rate and temperature, as shown in Figures 4(a) through (c). The predicted flow stress shows satisfactory agreement with the experimental results with an accuracy of $R^2 = 0.955$, as shown in Figure 4(d). The prediction is good at a low strain rate. However, a considerable amount of error has been observed for low strain with high-strain rate data, Figure 4(a).

C. Microstructure of the As-Cast Sample

A scanning electron micrograph of the as-cast sample, prepared by the arc melting technique, is shown in Figure 5(a). Small precipitates are found to be embedded inside the matrix. The microstructure mainly consists of two phases, a disordered FCC matrix (γ) and an ordered L12 precipitate (γ'), as confirmed by

XRD analysis, shown in Figure 5(b) (see electronic supplementary Figure S2 for the corresponding phase diagram). The weak intensity of the ordered γ' phase signifies the lower volume fraction of that phase. The volume fraction of ordered precipitates is expected to be less than 5 pct. The evolution of ordered L12 precipitate (γ') in this alloy was also reported by Yeh *et al.* and Te-Kang Tsao *et al.*^[17,19] in different studies. However, the volume fraction of the order phase in the present study is found to be less as compared to the volume fraction of the order phase reported in those studies. EBSD analysis has been carried out on the as-cast to reveal further microstructural and microtextural information. The inverse pole figure map of the as-cast sample is represented in Figure 6(a). The as-cast alloy consists of larger grain which is unevenly distributed throughout the scanned area. The grain size distribution of the investigated sample is shown in Figure 6(b). The average grain size is found to be around 390 ± 120 microns. As expected for the as-cast sample, all the grain boundaries are found to be high angle (> 15 deg) in nature, as shown in Figure 6(c).

D. Microstructural and Texture Analysis of the Hot Deformed Sample

In order to understand the overall flow behavior, the microstructural and microtextural study has been carried out after the hot deformation. EBSD scans are performed on the plane containing compression direction at the center portion of the deformed samples. The inverse pole figure maps of the investigated samples are shown in Figure 7. At a high-strain rate and low processing temperature, 1173 K and SR = 0.1. The grains are found to be deformed and elongated perpendicular to the compression direction. On the other hand, at high temperatures and low strain rates, 1373 K SR = 0.001, new equiaxed grains are found to evolve. These new equiaxed grains are the results of dynamic recrystallization. For further confirmation, the grain orientation spread (GOS) map of the investigated sample is constructed and shown in Figure 8. Fine grains are found to have a small GOS level and, thus, are a product of dynamic recrystallization. The extent of

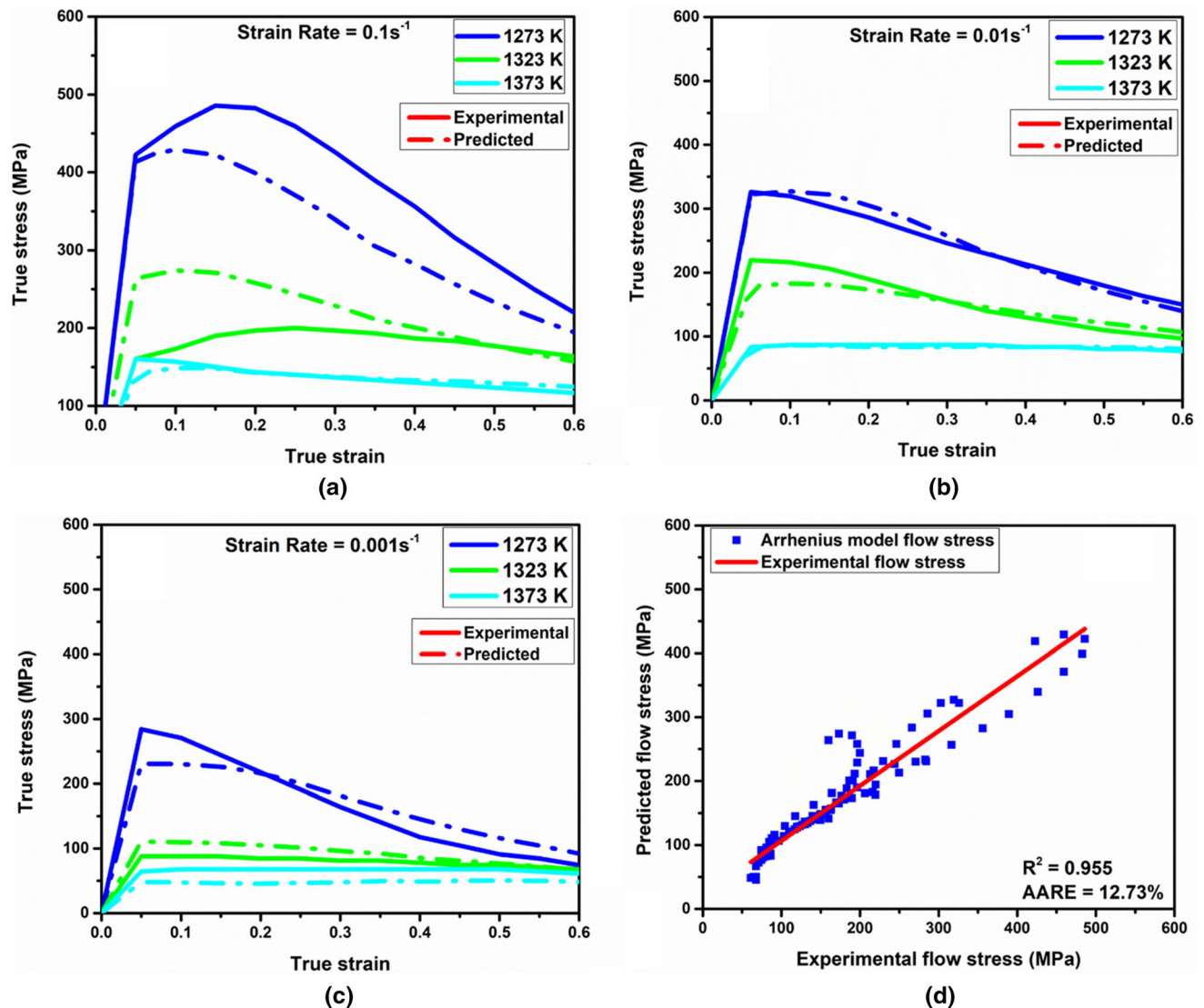


Fig. 4—Comparison between the experimental and predicted flow stress data using the Arrhenius model at different strain rates.

dynamic recrystallization depends on the deformation temperature and strain rate; therefore, the fraction of recrystallized grain varies depending on the processing conditions. In order to quantify the fraction of recrystallized grain, a threshold GOS of 0.1 deg was considered, and grains having less than 0.1 deg GOS are considered as recrystallized grain. The subset of dynamic recrystallized grain is shown in Figure 9. The fraction of recrystallized grain is negligible (< 2 pct) in the case of 1173 K and SR = 0.1. Recrystallized equiaxed grains are found to start evolving from the grain boundary region. The triaxial state of stress at the grain boundary might have promoted dynamic recrystallization at the grain boundary region. Percentage of dynamically recrystallized grains increases with the increase in temperature and with the decrease in the strain rate of the deformation. At the temperature of 1373 K and the fraction of recrystallized (DRX), grains are more than 60 pct, even at a strain rate of 0.1. The average recrystallized grain size was $5.82 \pm 1.7 \mu\text{m}$.

Grain growth after dynamic recrystallization has also been observed at higher temperatures and lower strain rates. The grain growth phenomenon is quite prominent in sample of 1323 K and SR = 0.01, where the recrystallized fraction is 58 pct, and the average grain size is around $20.35 \pm 7.09 \mu\text{m}$. Higher holding time and at high temperature may have contributed to grain growth in these samples.

An attempt has been made to study the deformation and recrystallization texture of the investigated samples. IPF map with respect to compression direction (CD) has been constructed after taking a subset of the recrystallized and deformed grain, as shown in Figure 10. We could not detect any trend in the deformed texture with respect to deformation temperature and strain rate. In most cases, the selected region for EBSD analysis is covered by a few deformed grains and may not be statistically enough to comment on the overall texture development in the deformed grains. On the other hand, a clear trend of a decrease in texture index or weak

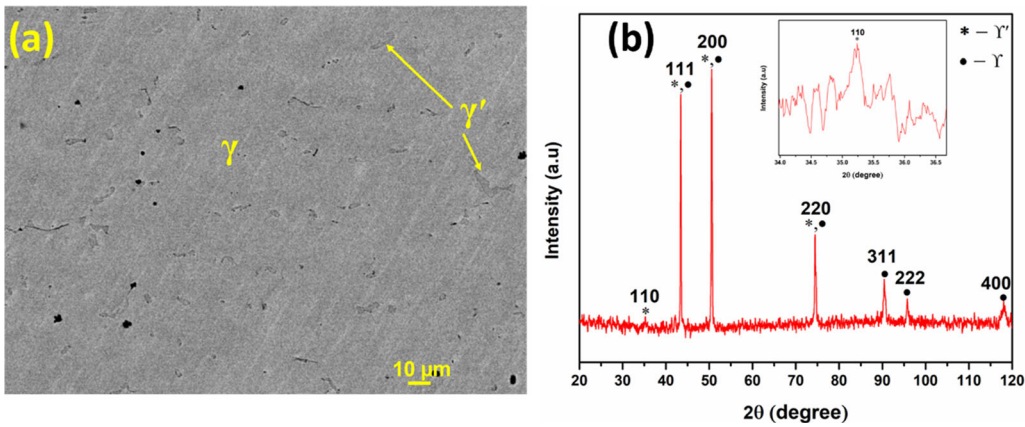


Fig. 5—(a) SEM of as-cast sample (b) XRD Analysis.

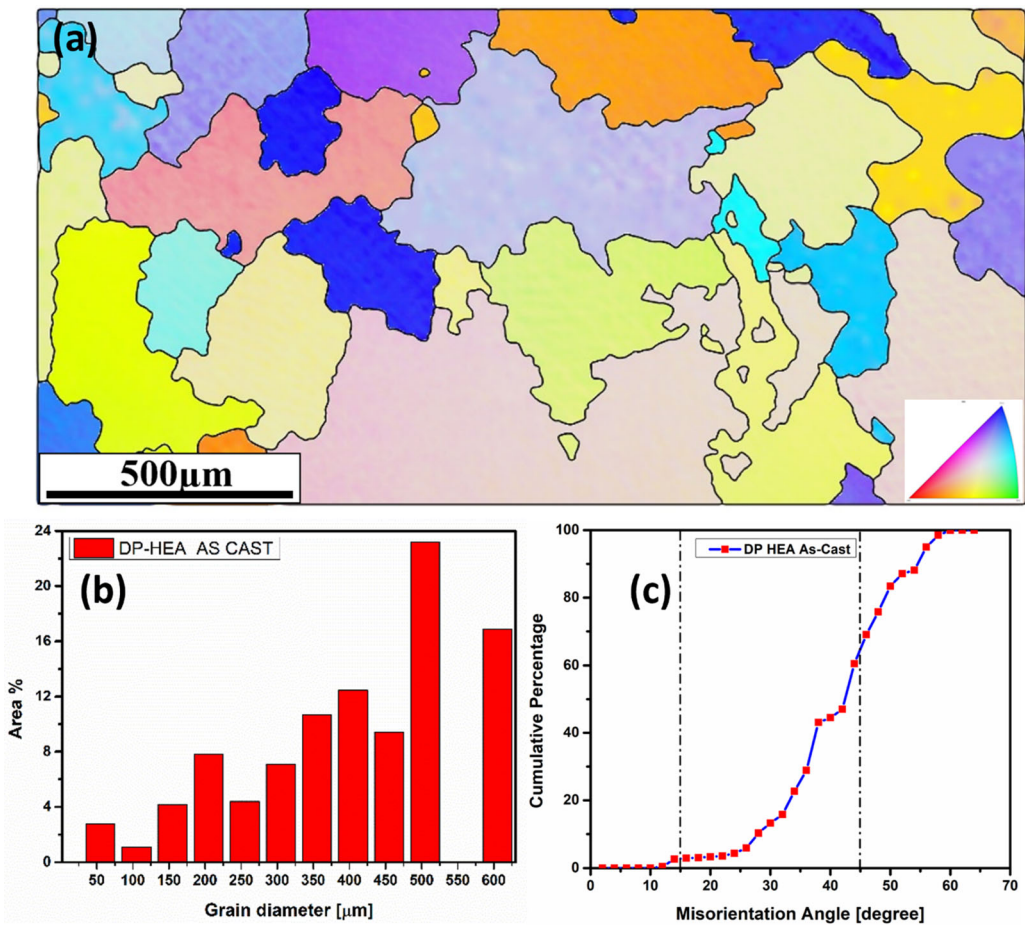


Fig. 6—(a) Inverse pole figure mapping (b) grain size distribution (c) misorientation angle distribution.

texture has been observed in the recrystallized grains. In order to understand the deformation texture, macrotexture analysis has been carried out for the sample tested at 1173 K, where the fraction of recrystallized grain is negligible (< 2 pct). Inverse pole figures with respect to compression direction (CD) of the investigated samples

are shown in Figure 11. In all the samples, fiber texture having $CD \parallel \langle 001 \rangle$ has been observed. In the case of the lowest strain rate of 0.001, the presence of an additional texture component $CD \parallel \langle 111 \rangle$ has also been found.

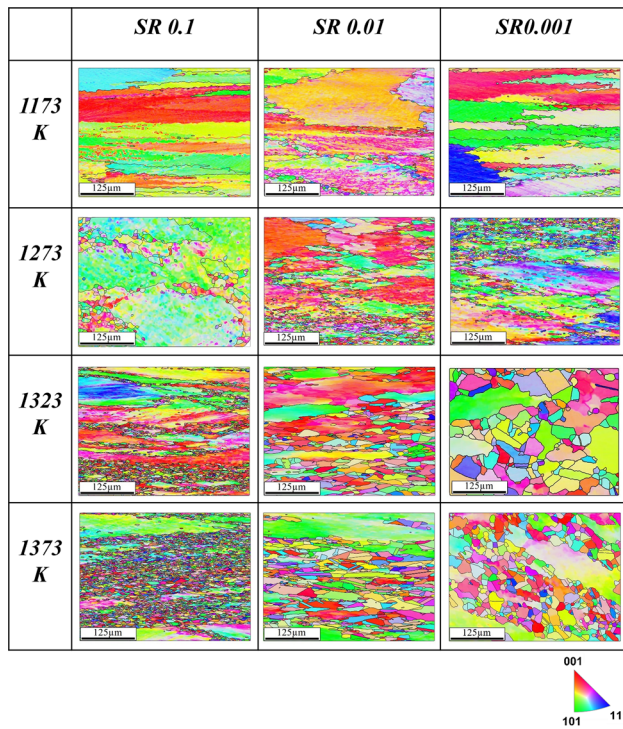


Fig. 7—EBSD inverse pole figure (IPF) maps of the specimens hot compressed specimen compressed at different strain rates and temperatures.

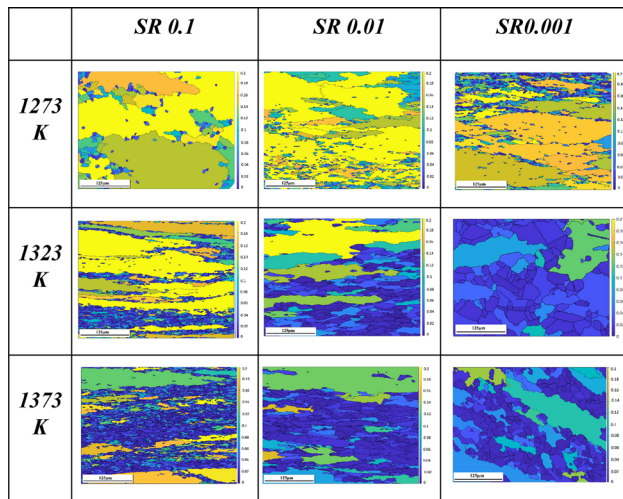


Fig. 8—Grain orientation spread (GOS) maps of the specimens hot compressed specimen compressed at different strain rates and temperatures.

IV. DISCUSSION

The flow curve of investigated samples shows significant softening after the initial hardening period. The flow hardening effect was short and limited within a small strain (< 0.05 strain) in most of the investigated samples tested on or above 1273 K except for 1273 K, SR = 0.1 and 1323 K, SR = 0.1 samples. In those samples, shorter holding time (due to the highest strain rate of 0.1) may have contributed to the development of

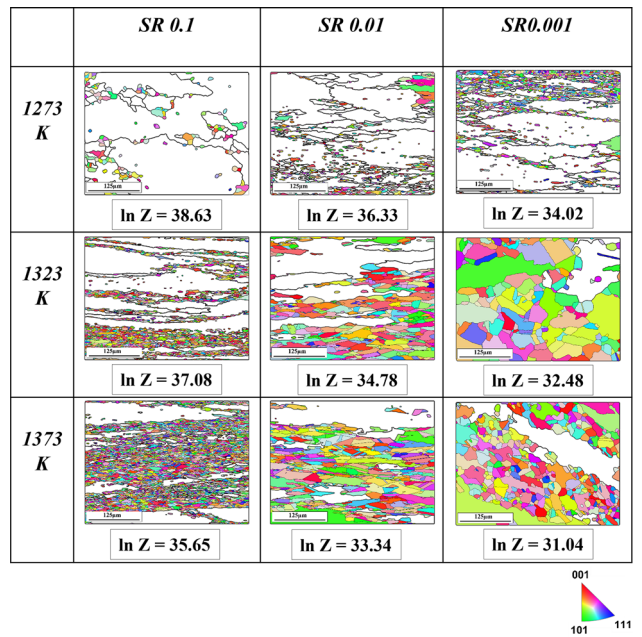


Fig. 9—Grain orientation spread (GOS < 0.1) maps of the specimens hot compressed specimen compressed at different strain rates and temperatures.

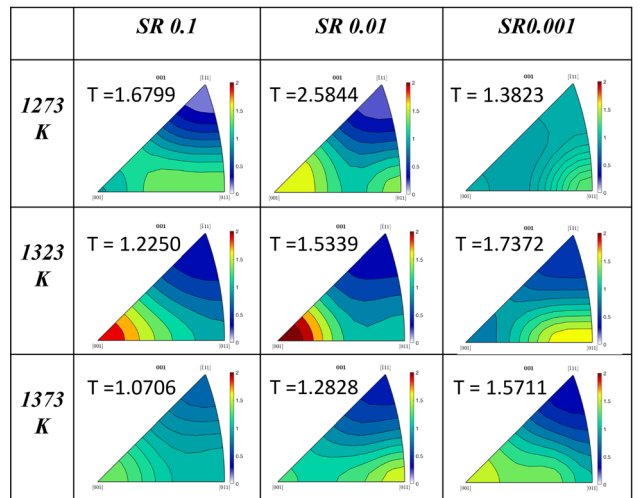


Fig. 10—Inverse pole figure (IPF) obtained from the EBSD data depicting the crystallographic texture parallel to the compression Axis (CA) for the recrystallized region (GOS = 0.1). T shows the texture index of each IPF plot.

a wide range of hardening zone. On the other hand, in the case of a lower strain rate (0.01 s^{-1} and 0.001 s^{-1}), longer holding time is expected to annihilate the dislocation substructure or low angle boundary and reduce the hardening effect.

Several factors are found to contribute to the flow softening behavior, such as the formation of cracks and dynamic recrystallization. The flow softening is highest in the samples hot deformed at 1173 K (as shown in Figure 1) among all the samples. Microstructural analysis reveals that the percentage of dynamic recrystallized

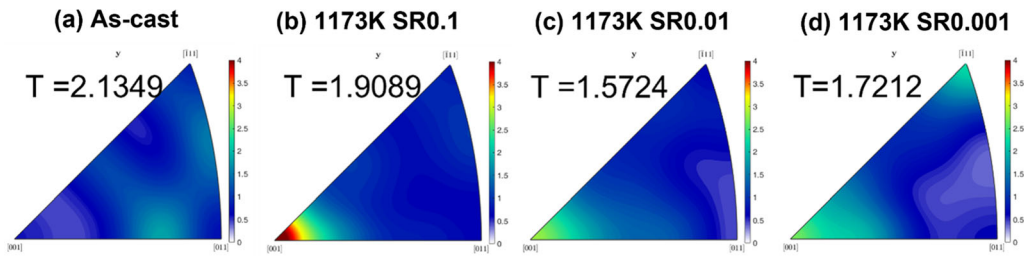


Fig. 11—Macrotexture analysis of (a) As-cast sample, (b), (c), and (d) sample deformed at 1173 K, T indicates the texture index.

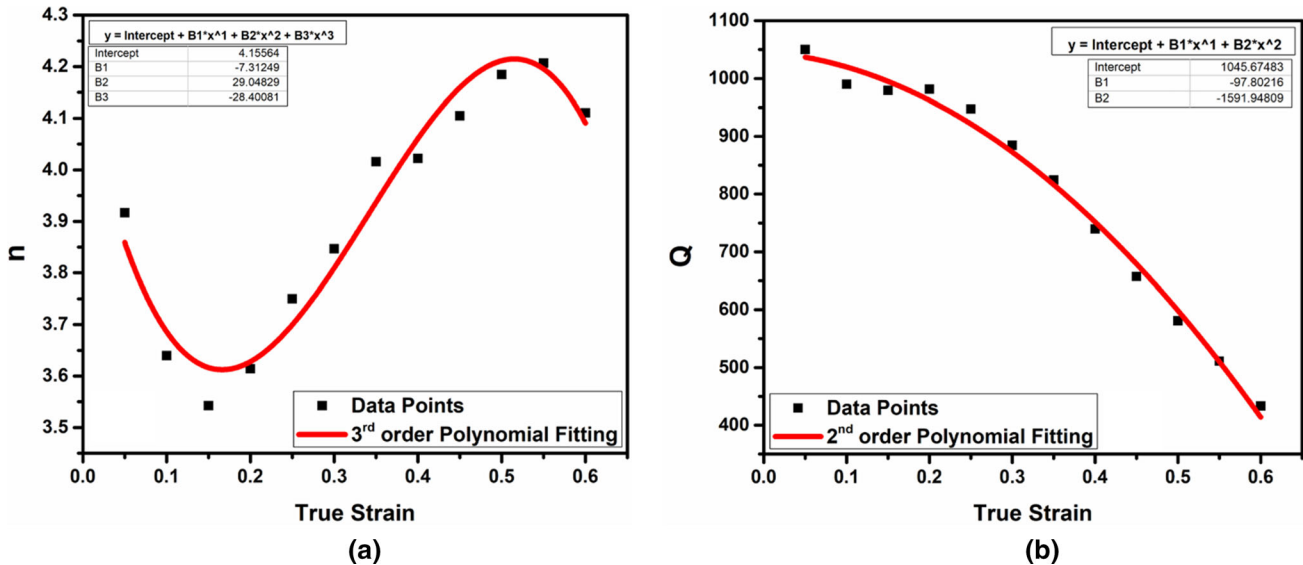


Fig. 12—Variation of parameters (a) n and (b) Q with true strain.

grain is negligible (< 2 pct) in those samples. Therefore, dynamic recrystallization should not be the primary reason behind observed softening in those samples, and flow softening is mainly due to the development of cracks (as shown in Figure 2). The maximum flow stress of the samples deformed at 1173 K is high, *i.e.*, above 600 MPa. In addition, due to the absence of DRX in these samples, the microstructures consist of coarse grains (mean grain size is greater than $90 \mu\text{m}$), Figure 7. These factors might have contributed to the development of severe through-thickness crack in the central region of samples, deformed at 1173 K.

In the present work, an attempt has been made to predict the flow stress at different deformation conditions using the constitutive equation based on the sine hyperbolic function of stress. The obtained stress exponent ' n ' and activation energy Q at different strain rates are shown in Figure 12. At all strain levels (0.05 to 0.6), the obtained ' n ' value Figure 12(a) is found to be above 3, which implies the deformation mechanism is related to dislocation climb. The estimated activation energy is found to decrease with strain, as shown in Figure 12(b). This decreasing trend suggests the occurrence of dynamic recrystallization.^[24] Strain-free microstructure, after dynamic recrystallization, facilitates easy movement of dislocation and thereby reduces

the activation barrier. The activation energy reduces to 433 kJ/mol at a 0.6 strain. The activation barrier for self-diffusion of Fe, Co, Ni, Cr, Al, and Ti is 309 kJ/mol, 270 kJ/mol, 304 kJ/mol, 313 kJ/mol, 142 kJ/mol, and 303 kJ/mol, respectively.^[24–26] Here, the estimated value of activation energy is higher than the activation energy of self-diffusion of the individual elements. This indicates some part of the activation barrier is mechanically driven.^[24]

Electron backscattered diffraction (EBSD) analysis on the hot deformed sample, as shown in Figure 7, confirms the occurrence of DRX. Small grains developed as a result of dynamic recrystallization are strain free with very low GOS value. The fraction of recrystallized grains is found to increase with increasing temperature and decreasing strain rate, Figure 9. In order to combine the effect of both strain rate and temperature, the Zener Holloman parameter has been introduced. The percentage of dynamic recrystallized grain vs Zener Holloman parameter is shown in Figure 13. Overall, the volume fraction of recrystallized grain is found to decrease with an increase in $\ln(Z)$. A similar observation has been reported in other studies.^[8] The grain size of the recrystallized sample has been calculated separately, as shown in Figure 14. Clearly, in the case of low strain rate and high temperature, there is a considerable

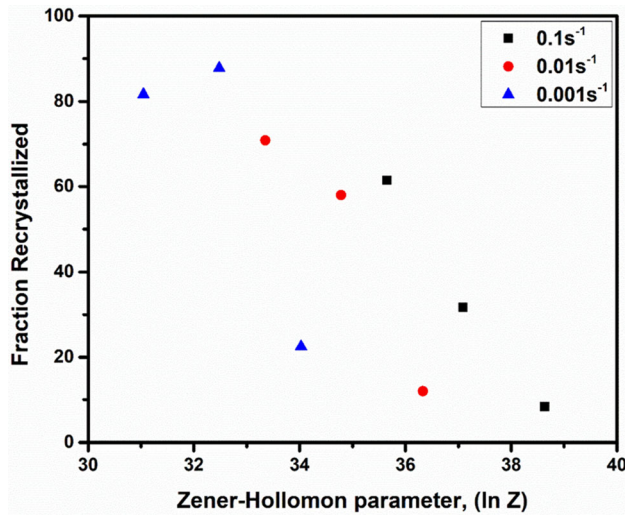


Fig. 13—Effect of Zener Hollomon parameter on the recrystallized fraction.

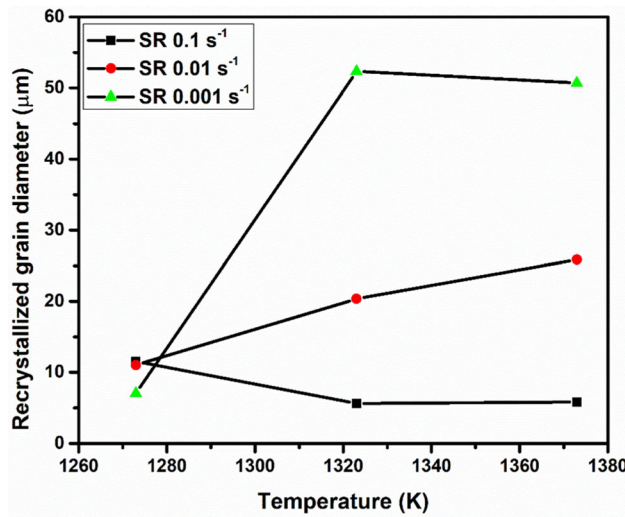


Fig. 14—Variation of recrystallized grain size w.r.t. temperature.

amount of grain growth. Therefore, intermediate deformation temperature and high-strain rate are expected to provide the best condition for uniform deformation since the microstructure contains optimum DRX with negligible grain growth.^[27]

In order to understand the overall hot deformation mechanism, crystallographic texture has been analyzed in detail. The texture index of the recrystallized region of the deformed sample is lower when compared to the as-cast sample. It indicates that the development of random texture is due to dynamic recrystallization. Some other studies also made similar observations on dynamic recrystallized samples.^[2,8] It can also be concluded that orientation-dependent grain growth did not occur. On the other hand, two different types of texture, such as $CD \parallel \langle 001 \rangle$ and $CD \parallel \langle 111 \rangle$, have been found to evolve in deformation texture at 1173 K.

Further in-depth analysis is required for a complete understanding of deformation texture.

V. CONCLUSIONS

The microstructural and textural evolution during the hot deformation of the FeCoNiCrAlTi dual-phase HEA in the large range of processing parameters is studied, and the flow stress prediction is aided with the help of numerical simulations. After the analysis of the obtained results, the following conclusions were drawn:

- (i) Sine hyperbolic-based constituent equations depicting the relationship between the flow stress and strain rate with deformation temperature at 0.6 true strain are as follows:

$$\dot{\epsilon} = 7.14 \times 10^{14} \times [\sinh(0.009252 \times \sigma_{0.6})]^{4.11} \times \exp\left(\frac{433253}{RT}\right)$$

$$\sigma_{0.6} = \frac{1}{0.009252} \ln\left(\left(\frac{Z_{0.6}}{7.14 \times 10^{14}}\right)^{\frac{1}{4.11}} + \left(\left(\frac{Z_{0.6}}{7.14 \times 10^{14}}\right)^{\frac{2}{4.11}} + 1\right)^{\frac{1}{2}}\right)$$

The Arrhenius-type sine hyperbolic constitutive equation predicts the flow stress with an accuracy of $R^2 = 0.955$ at the strain 0.6. The estimated activation energy at 0.6 strain is 433.25 kJ/mol.

- (ii) The reduction of the flow stress in the flow curve after attaining the peak stress is mainly because of two reasons, *i.e.*, because of the formation of cracks when the material is deformed at low temperature and because of the occurrence of dynamic recrystallization at higher temperature deformation, which has already been supported by the microstructural observation.
- (iii) Initially, the formation of the recrystallized grains starts near the grain boundary and starts to form a necklace kind of structure. Furthermore, the size of the recrystallized grains increases with an increase in temperature and decrement in strain rate. The volume fraction of the recrystallized grains is found to decrease with an increase in the Zener Holloman parameter.
- (iv) Random texture is found to evolve during dynamic recrystallization, and the overall texture index reduces because of DRX.

CONFLICT OF INTEREST

No potential conflict of interest was reported by the authors.

SUPPLEMENTARY INFORMATION

The online version contains supplementary material available at <https://doi.org/10.1007/s11661-023-07093-x>.

REFERENCES

1. J. Yeh, S. Chen, S. Lin, J. Gan, T. Chin, T. Shun, and C. Tsau: *Adv. Eng. Mater.*, 2004, vol. 5, pp. 299–303.
2. N. Prasad, N. Bibhanshu, N. Nayan, G.S. Avadhani, and S. Suwas: *J. Mater. Res.*, 2018, vol. 34, pp. 1–2.
3. M. Tsai and J. Yeh: *Mater. Res. Lett.*, 2014, vol. 2, pp. 37–41.
4. T.K. Tsao, A.C. Yeh, C.M. Kuo, and H. Murakami: *Entropy*, 2016, vol. 18, pp. 1–3.
5. Y. Zhang, T.T. Zuo, Z. Tang, M.C. Gao, K.A. Dahmen, P.K. Liaw, and Z.P. Lu: *Prog. Mater. Sci.*, 2014, vol. 61, pp. 1–93.
6. K.Y. Tsai, M.H. Tsai, and J.W. Yeh: *Acta Mater.*, 2013, vol. 61, pp. 4887–97.
7. F. Otto, Y. Yang, H. Bei, and E.P. George: *Acta Mater.*, 2013, vol. 61, pp. 2628–38.
8. R.R. Eleti, T. Bhattacharjee, L. Zhao, P.P. Bhattacharjee, and N. Tsuji: *Mater. Chem. Phys.*, 2018, vol. 210, pp. 176–86.
9. S. Guo and C.T. Liu: *Prog. Nat. Sci. Mater. Int.*, 2011, vol. 21, pp. 433–46.
10. O.N. Senkov and D.B. Miracle: *J. Alloys Compd.*, 2016, vol. 658, pp. 603–07.
11. Y. Zhang, Y.J. Zhou, J.P. Lin, G.L. Chen, and P.K. Liaw: *Adv. Eng. Mater.*, 2008, vol. 10, pp. 534–38.
12. A. Shafiee, M. Nili-Ahmadabadi, H.S. Kim, and M. Jahazi: *Met. Mater. Int.*, 2020, vol. 26, pp. 591–602.
13. R. C. Reed, *The Superalloys*, Cambridge University Press, Cambridge, 2006.
14. S. Chen, Q. Li, J. Zhong, F. Xing, and L. Zhang: *J. Alloys Compd.*, 2019, vol. 791, pp. 255–64.
15. R.C. Reed, T. Tao, and N. Warnken: *Acta Mater.*, 2009, vol. 57, pp. 5898–5913.
16. R.A. Hobbs, S. Tin, and C.M.F. Rae: *Metall. Mater. Trans. A*, 2005, vol. 36, pp. 2761–73.
17. A. C. Yeh, T. K. Tsao, Y. J. Chang, K. C. Chang, J. W. Yeh, M. S. Chiou, S. R. Jian, C. M. Kuo, W. R. Wang, and H. Murakami: *Int. J. Metall. Mater. Eng.*, vol. 1, pp. 107.
18. T.K. Tsao, A.C. Yeh, C.M. Kuo, K. Kakehi, H. Murakami, J.W. Yeh, and S.R. Jian: *Sci. Rep.*, 2017, vol. 7, p. 12658.
19. T.K. Tsao, A.C. Yeh, C.M. Kuo, and H. Murakami: *Adv. Eng. Mater.*, 2017, vol. 19, p. 1600475.
20. T. Tsao, A. Yeh, and H. Murakami: *Metall. Mater. Trans. A*, 2017, vol. 48A, pp. 2435–42.
21. R. Jain, M.R. Rahul, P. Chakraborty, R.K. Sabat, S. Samal, G. Phanikumar, and R. Tewari: *J. Alloys Compd.*, 2021, vol. 888, 161579.
22. Z.S. Motlagh, B. Tolaminejad, and A. Momeni: *Met. Mater. Int.*, 2021, vol. 27, pp. 2512–29.
23. Y.C. Lin and X.M. Chen: *Mater. Des.*, 2011, vol. 32, pp. 1733–59.
24. R. Sonkusare, A. Swain, M.R. Rahul, S. Samal, N.P. Gurao, K. Biswas, S.S. Singh, and N. Nayan: *Mater. Sci. Eng. A*, 2019, vol. 759, pp. 415–29.
25. Y. Sun, Q. Pan, Z. Huang, W. Wang, X. Wang, M. Li, and J. Lai: *Prog. Nat. Sci. Mater. Int.*, 2018, vol. 28, pp. 635–46.
26. L. Badea, M. Surand, J. Ruau, B. Viguier, L. Badea, M. Surand, J. Ruau, and B. Viguier: *Univ. Polytechnica Bucharest Sci. Bull. Series B*, 2014, vol. 76, pp. 185–96.
27. A. Chaudhuri, A.N. Behera, A. Sarkar, R. Kapoor, R.K. Ray, and S. Suwas: *Acta Mater.*, 2019, vol. 164, pp. 153–64.

Publisher's Note Springer Nature remains neutral with regard to jurisdictional claims in published maps and institutional affiliations.

Springer Nature or its licensor (e.g. a society or other partner) holds exclusive rights to this article under a publishing agreement with the author(s) or other rightsholder(s); author self-archiving of the accepted manuscript version of this article is solely governed by the terms of such publishing agreement and applicable law.